Graphene thermal infrared emitters integrated into silicon photonic waveguides – Supporting Information

Nour Negm[1,2], *Sarah Zayouna*[3], *Shayan Parhizkar*[1,2], *Pen-Sheng Lin*[4], *Po-Han Huang*[4], *Stephan Suckow*[1], *Stephan Schroeder*[3], *Eleonora De Luca*[3], *Floria Ottonello Briano*[3], *Arne Quellmalz*[4], *Georg S. Duesberg*[5], *Frank Niklaus*[4], *Kristinn B. Gylfason*[4], *Max C. Lemme*[1,2*]

[1]AMO GmbH, Advanced Microelectronic Center Aachen, Otto-Blumenthal-Str. 25, 52074 Aachen, Germany

[2]Chair of Electronic Devices (ELD), RWTH Aachen University, Otto-Blumenthal-Str. 25, 52074 Aachen, Germany

[3]Senseair AB, Stationsgatan 12, 824 08 Delsbo, Sweden

[4]Division of Micro- and Nanosystems, School of Electrical Engineering and Computer Science, KTH Royal Institute of Technology, 100 44 Stockholm, Sweden

[5]Institute of Physics, Faculty of Electrical Engineering and Information Technology (EIT 2), Bundeswehr University Munich, Werner-Heisenberg-Weg 39, 85577 Neubiberg, Germany

*Email: max.lemme@rwth-aachen.de

Number of pages: 16

Number of figures: 12

SI1 – EXPERIMENTAL LOSS EXTRACTION USING THE CUTBACK METHOD

Figure S1 illustrates the WG propagation and GC coupling losses extracted employing the so-called cutback measurement method. For that, dedicated test structures of different waveguide lengths between 1.1 mm and 4 mm, with grating couplers on each side, are characterized using an external quantum cascade laser emitting at 4.23 µm wavelength and a suitable single-pixel detector in a fiber-coupled setup.

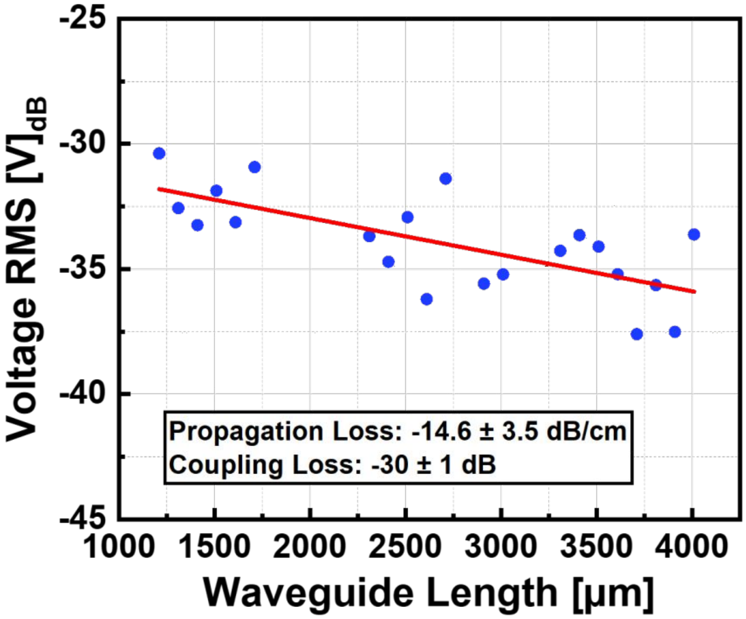

Figure S1. Cut-back method result measured at $\lambda = 4.2$ µm, plotting the RMS voltage at the detector in dB versus the length of different test waveguides to determine the propagation loss (slope) and total coupling loss (y-intercept).

SI2 – NUMERICAL SIMULATION OF THE GRATING COUPLER PERFORMANCE

The outcoupling efficiency of the grating couplers was simulated with Ansys Lumerical FDTD in the camera sensitivity range from 3 to 5 µm wavelength and is shown in Figure **S2**.

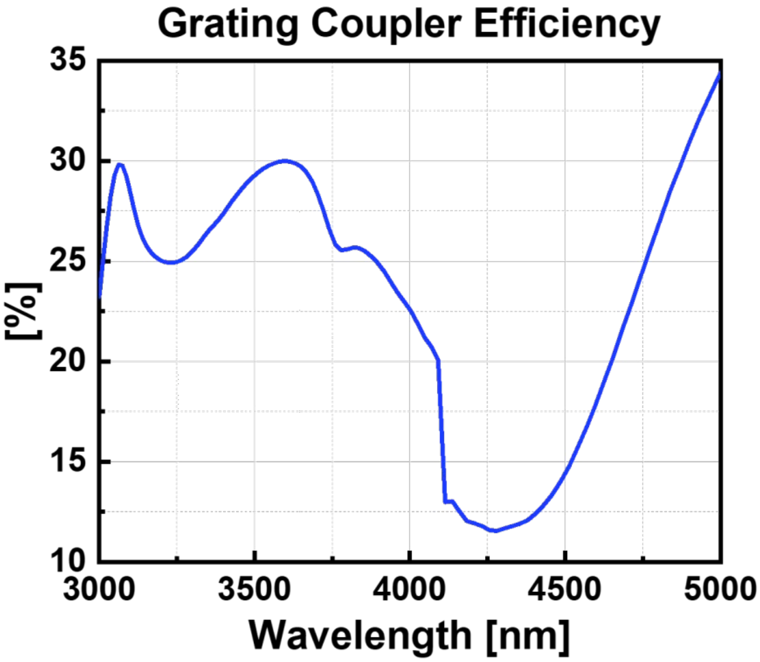

Figure S2. Grating coupler efficiency, calculated using Ansys Lumerical FDTD, in the wavelength range of 3 to 5 µm.

SI3 – IR CAMERA CALIBRATION MODES AND CURRENT LIMITATIONS

The IR camera used in our measurements supports five different calibration modes for the data output from the camera: **Raw** (no correction), **Non-uniformity Correction** (NUC), **Radiometric-Temperature** (RT), **in-band Radiance** (IBR), and **in-band Irradiance** (IBI).

The **raw data** represents the camera's unaltered output. This data usually shows pixel gain and offset non-uniformity, which is why it can rarely be used for analysis.

The **non-uniformity correction NUC data** applies a gain and offset correction to the raw data on a pixel-by-pixel basis so that a uniform scene like blackbody should give a uniform digital level measurement. As a count-based quantity, NUC measurements are typically proportional to exposure time for a constant scene. We have used the NUC calibration mode for the majority of our data, especially in Figures 2 and 3 in our manuscript.

The **radiometric temperature RT data** effectively represents the temperature of a perfect blackbody for each pixel that would create the signal measured by that pixel. As this is done on a pixel-by-pixel basis, RT performs non-uniformity correction and expresses the results in units of temperature (K). But as real objects are usually not perfect blackbodies and therefore have an emissivity lower than unity, this means that the radiometric temperature is usually lower than the real temperature of the object. This can be seen in our manuscript in the data of Figure 4a, where the IR camera data was saved in this calibration mode. The qualitative temperature values displayed here from around 300 to 400 K are significantly lower than the temperature range expected by our simulations (Figure 5c, 300 to 1300 K). The determination of the real thermodynamic temperature of an object with our IR camera is a process that requires good knowledge of the object and environment. This means especially the exact knowledge of the emissivity of all materials involved as well as an understanding of reflections coming from our emitter and/or the environment. We do not have this quantitative knowledge at this point, at least not at the required confidence level to use the RT data quantitatively. Therefore, we had to display the emission data of our emitters in arbitrary units, reflecting that it is only available relatively.

The **in-band radiance IBR data** converts the radiometric temperature to radiance units (W/m²sr²) by multiplying Planck's law with the spectral response of the system and integrating over the effective wavelength band (3 to 5 µm). The **in-band irradiance IBI data** (units of W/m²) is a direct conversion from in-band radiance to account for the solid angle subtended by the camera detector.

We want to demonstrate the current restrictions of our IR camera calibration modes to further explain the use of NUC data in our manuscript. Figure S3 illustrates a replot of Figure 3 of our manuscript after converting our IR camera data to extract the apparent optical output powers of the emitter and grating coupler. For that, we have converted our data to IBI and, as the conversion is done on a pixel-by-pixel basis, multiplied the data with the chip area covered by one pixel.

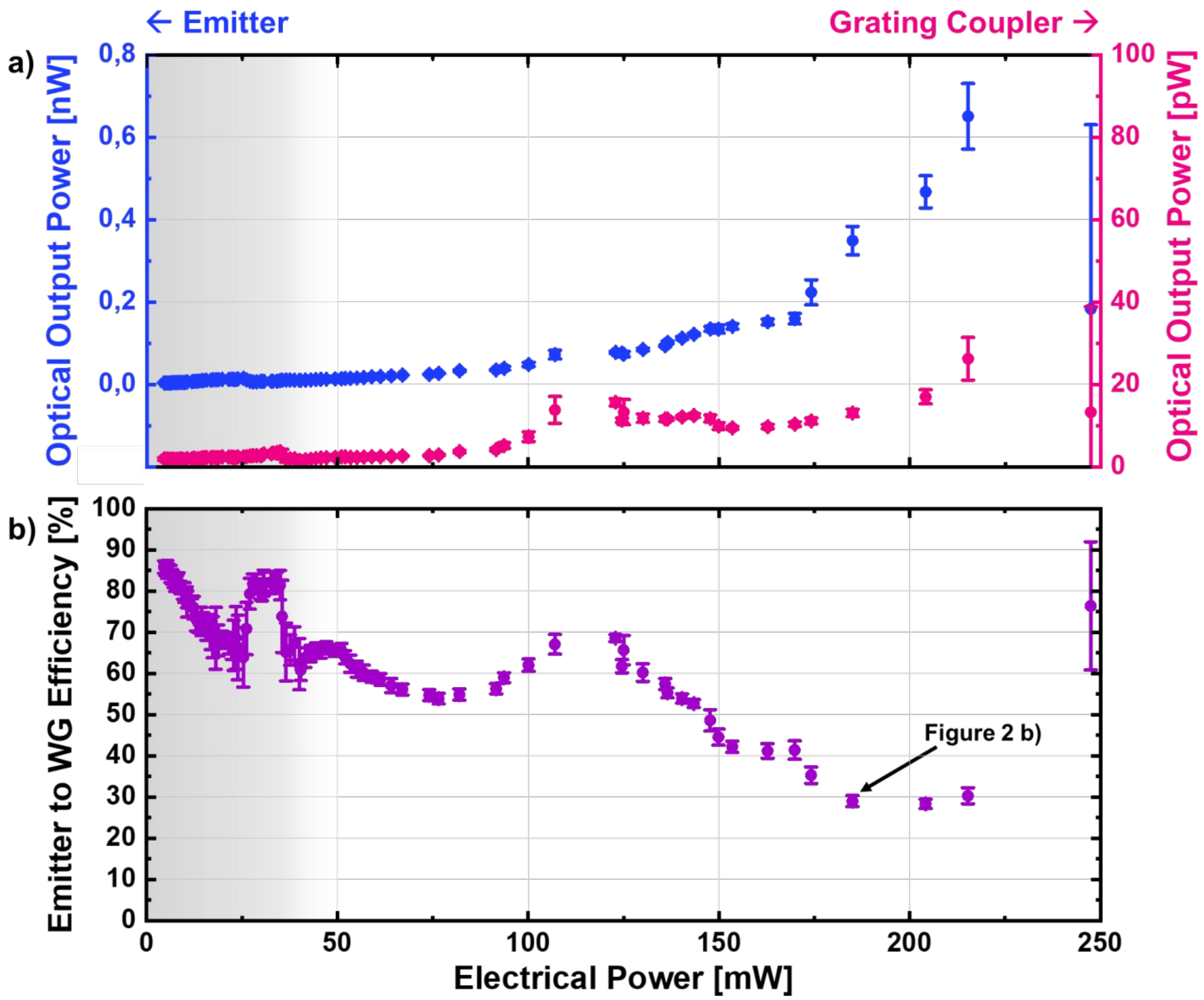

Figure S3. Replot of Figure 3 of our manuscript after converting our IR camera data to IBI.

Compared to Figure 3, as shown in our manuscript, generated out of NUC data, the IBI data exhibit the same linear behavior, resulting in an identical emitter-to-waveguide coupling efficiency calculation starting at 50 mW. However, as the IBI data is converted from the RT data, which is based on the behavior of a perfect blackbody, the resulting optical output powers of the emitter and the grating coupler are extremely small and cannot reasonably represent our graphene emitters. Therefore, the IBI data is also not representative for extracting the apparent output efficiency of the grating coupler and the emitter with respect to the total applied electrical power, as shown in Figure S4. This data in parts per billion is strongly misleading because it is based on the behavior of a perfect blackbody, which is obviously not the case in our experiment. Unfortunately, we do not have the necessary information needed to reliably convert the IR cameras NUC data to representative RT data. It is also not advisable to rely on literature or simulated data, because making the required assumptions leads to strongly misleading conclusions if they are not accurate.

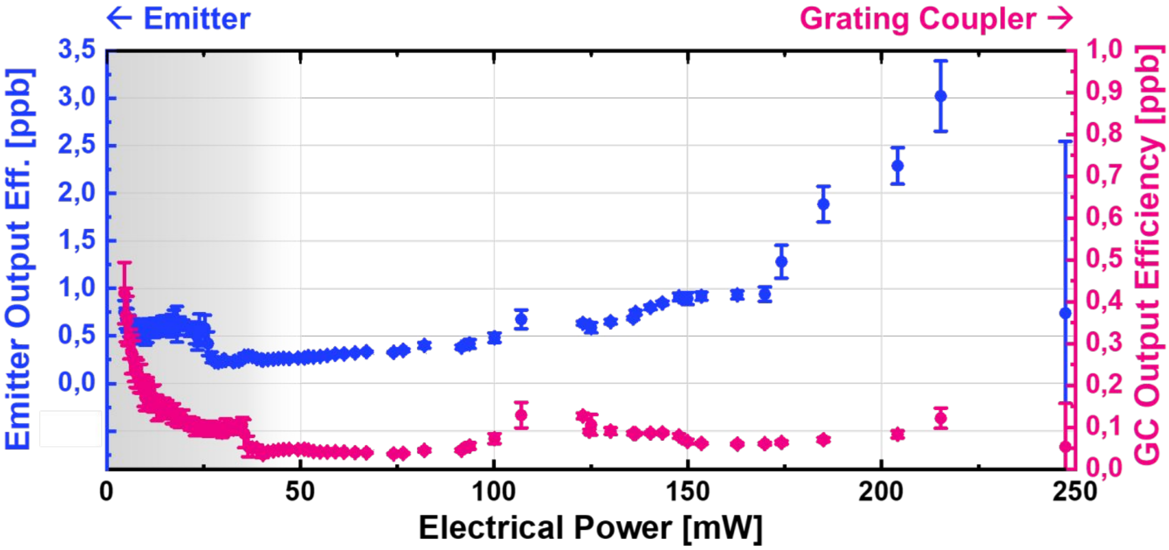

Figure S4. Apparent output efficiency of both the emitter and the grating coupler in parts per billion with respect to the total applied electrical power.

SI4 – INTERNAL EFFICIENCY OF THE ENTIRE OPTICAL SYSTEM

Figure **S5** illustrates the internal efficiency of the entire optical system of the emitter, waveguide, and grating coupler from the camera images as shown in Figure 2. The internal efficiency is defined as $\eta = I_{GC,out}/(I_{E,out} + I_{GC,out})$.

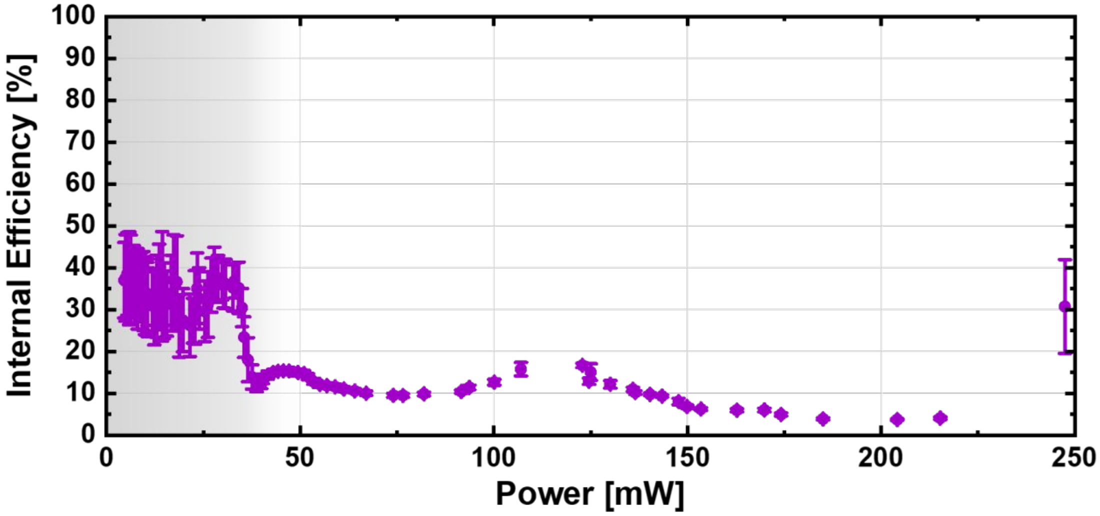

Figure S5. Internal efficiency $I_{GC,out}/(I_{E,out}+I_{GC,out})$ for the whole optical system of emitter, waveguide, and grating coupler.

SI5 – SIMULATION OF THE GRATING COUPLER EMISSION FRACTION AS DETECTED FROM THE IR CAMERA VS. WAVELENGTH

To further evaluate the measured emitter efficiency decrease with heating power, we used the Ansys Lumerical FDTD to calculate the fraction of grating coupler emission detected by the camera objective, limited by its numerical aperture. A WG source emitted light into the GC and a power monitor above the GC recorded the emission from the GC. The far field projection from this monitor yields the angle-resolved emission depending on wavelength. The peak emission angle varies from -20° at 5 μm wavelength to 40° at 3 μm wavelength. The IR camera has an acceptance angle of ±26.5°, which means that some emission at shorter wavelengths is not collected. Figure S3 shows the fraction of the emission which is captured by the camera, spectrally resolved.

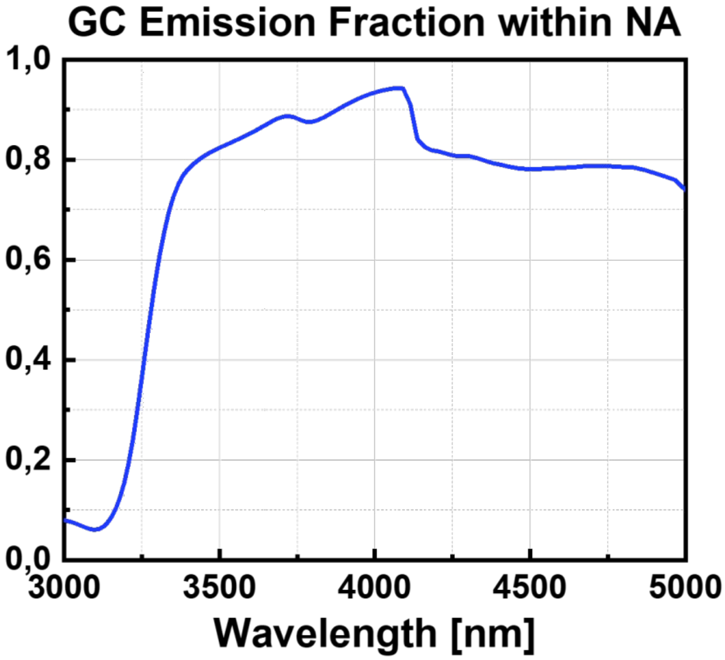

Figure S6. Grating coupler emission fraction as detected from the IR camera, calculated using Ansys Lumerical FDTD, in the wavelength range of 3 to 5 µm.

SI6 – QUANTITATIVE ANALYSIS OF THE ESTIMATED EMITTER EMISSION PROGRESSION WITH HEATING POWER

We attempt to give a more quantitative explanation of the estimated efficiency progression with heating power as illustrated in Figure 3. For that, we compare and relate any wavelength dependencies apparent for $I_{E,in}$ and $I_{E,out}$.

For $I_{E,in}$ to reach the IR camera, three parts of the optical system have to be taken into account, which can have wavelength-dependent efficiencies: waveguide, grating coupler, and numerical aperture of the camera. We have already quantified the latter two through simulations in supporting information SI2 and SI5. We have also extended our Lumerical simulation for the calculation of the waveguide losses in the range from 3 to 5 µm and confirmed the assumption in our manuscript that we can use the efficiency at 4.2 µm for the whole range to be valid.

Figure S7 illustrates the multiplication of the three efficiencies (waveguide (WG), grating coupler (GC), and numerical aperture (NA) of the camera) to analyze their combined impact.

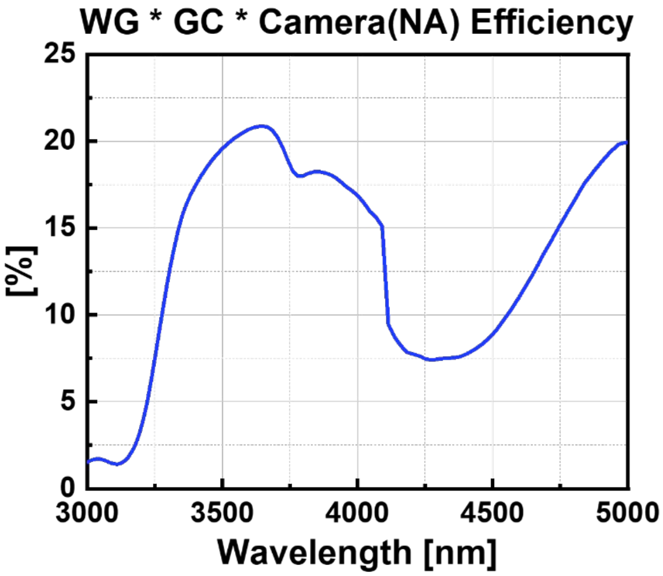

Figure S7. Multiplication of the efficiencies of waveguide, grating coupler and IR camera, calculated respectively using Ansys Lumerical FDTD, in the wavelength range of 3 to 5 μm.

Compared to $I_{E,in}$, we expect $I_{E,out}$ to go through a significantly less wavelength-dependent propagation path before reaching the IR camera. With a camera acceptance angle of ±26.5° and an angle of total reflection in Al_2O_3 of around 40° that is stable by ±2° for the wavelength range of 3 to 5 μm, we expect the impact of the numerical aperture of the camera to be relatively negligible for $I_{E,out}$. This means that Figure **S7** represents a combination of all strongly wavelength-dependent parts of the optical path.

In our manuscript, we assumed Wien's displacement law to offer a qualitative explanation of the measured efficiency decrease with heating power as the peak emission of the thermal emitter shifts to shorter wavelengths. We do not expect the efficiency of our emitter coupling into the waveguide to be completely wavelength independent, as the expansion of the mode decreases with shorter wavelengths. However, because the graphene is placed directly on top of the waveguides, we assume this to be less prominent in the progression of the efficiency compared to the wavelength-dependent optical paths summarized in Figure **S7**. Building on this assumption, the maximum apparent efficiency calculated in Figure 3b at 123 mW correlates with the maximum efficiency in Figure **S7** at a wavelength of around 3.5 to 4 µm. Below 123 mW, the peak emission of the thermal emitter must be at a wavelength above 4 µm, where the GC efficiency decrease is most prominent. Above 123 mW, the peak emission of the thermal emitter shifts to wavelengths under 3.5 µm, where the NA of the IR camera starts cutting off the emission from the grating coupler.

We try to further quantify and confirm our conclusions and assumptions. For that, we used the electro-thermal simulation (see Figure 5 in our manuscript) to extract the expected temperature of our emitter from Figure 3 with respect to the applied electrical power. We illustrate the results in Figure S8 for both the fully suspended and non-suspended model configurations as well as the temperature in between, as we expect for our emitters.

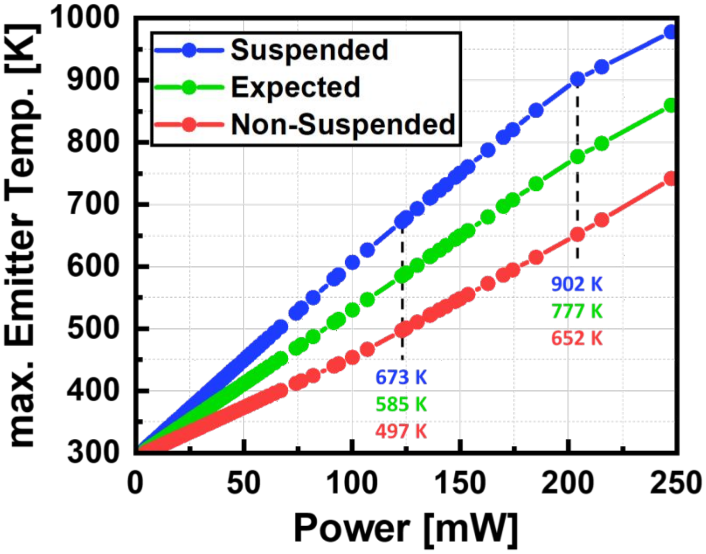

Figure S8. Expected maximum temperature of our emitter from Figure 3 with respect to the applied electrical power.

Next, we applied Planck's Law to obtain the radiation of a perfect blackbody in the range of 3 to 5 µm with respect to the electrical power applied to that emitter. Figure S9 illustrates this for the expected temperature profile (green data in Figure S8).

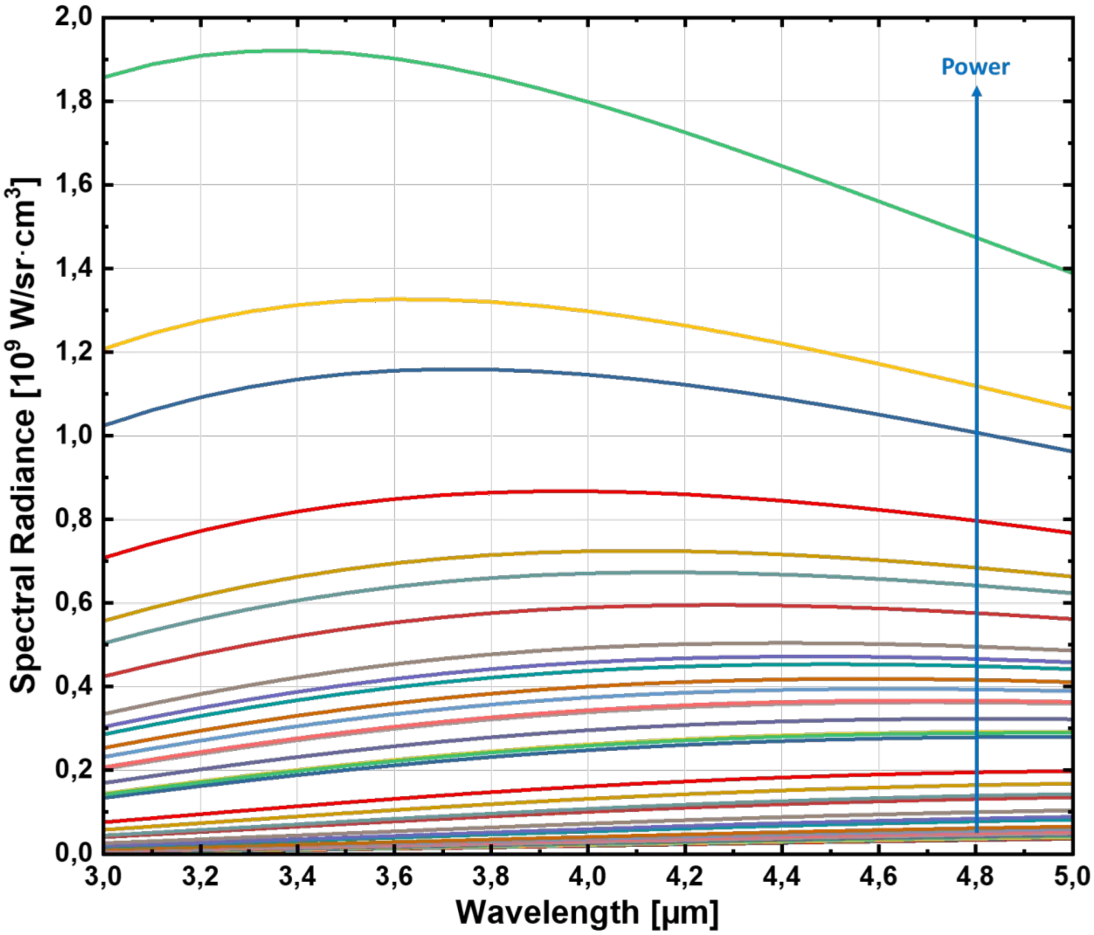

Figure S9. Radiation of a perfect blackbody in the range of 3 to 5 µm with respect to the electrical power applied to our emitter from Figure 3.

Figure S9 shows how the peak emission of the thermal emitter shifts to shorter wavelengths with higher temperatures, as stated by Wien's displacement law. Figure R8 illustrates at which wavelength the blackbody radiation of the emitter reaches its maximum in the acceptance range of the IR camera (3 to 5 µm) with respect to the applied electrical power, depending on the chosen model configuration.

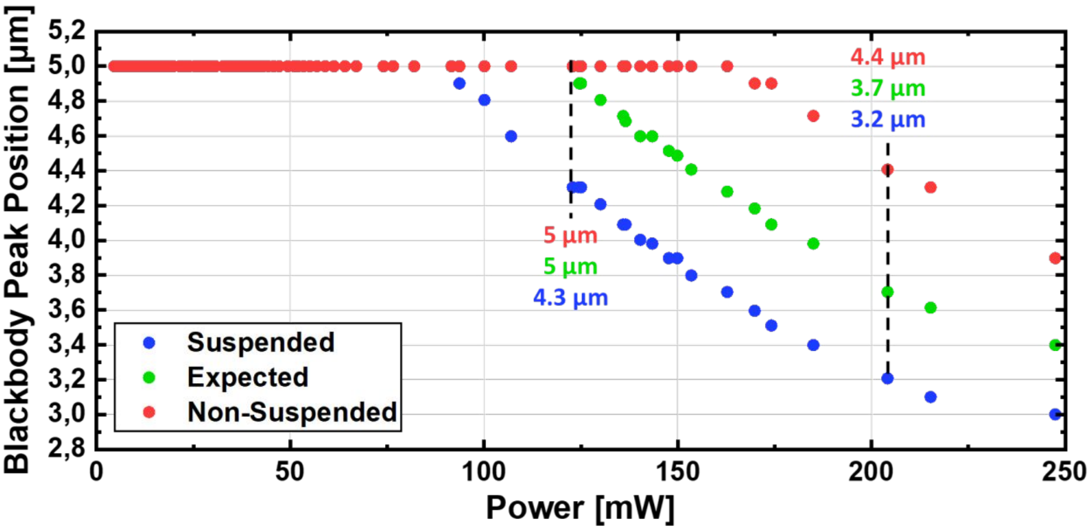

Figure S10. Position of the blackbody radiation peak, in the range from 3 to 5 µm, with respect to the applied electrical power.

The fully suspended simulated graphene model (blue) comes closest to a maximum apparent efficiency calculated in Figure 3b at 123 mW correlating with the maximum efficiency in Figure S7 at a wavelength of around 3.5 to 4 µm. However, if our assumptions are correct, we would expect even higher temperatures from our emitters than the simulation suggests. Unfortunately, we have no direct way to confirm this for our devices, as they have been destroyed in the course of the experiments. We also cannot provide more quantitative explanations about the efficiency without acquiring the spectra of the grating coupler and emitter emission to calculate the wavelength-dependent efficiency. It also needs to be noted that this attempt of a quantitative explanation is based too much on simulated data which could lead to significant uncertainties. In particular, small changes in temperature have a large effect on our data, as the power emitted by a blackbody scales with the fourth power of the temperature.

SI7 – INVESTIGATION OF THE POSSIBLE BREAKDOWN MECHANISMS

The breakdown mechanisms of the devices were investigated *post-mortem* through SEM images (Figure S11). Two breakdown areas have been identified commonly: the contact edges and the edges of the rib waveguides. The former indicates a high resistance of our bottom contacts to graphene. The latter can be attributed to the hot spots identified in the electro-thermal simulation, which may also be present in the actual sample to some extent. Additional defects or stress at the 50 nm step of the WG may further increase the resistance locally and hence lead to higher heating power and earlier breakdown. Some SEM images before breakdown also show other defects in the graphene, like folds in the graphene sheet or residues/particles (Figure S12). Some of these can be expected to create additional local hotspots. The simulation does not include such defects and hence probably underestimates the maximum temperatures reached. It is thus plausible that material starts to melt, as the SEM images in Figure S11 suggest, despite “only” 1000 K being reached in the simulation.

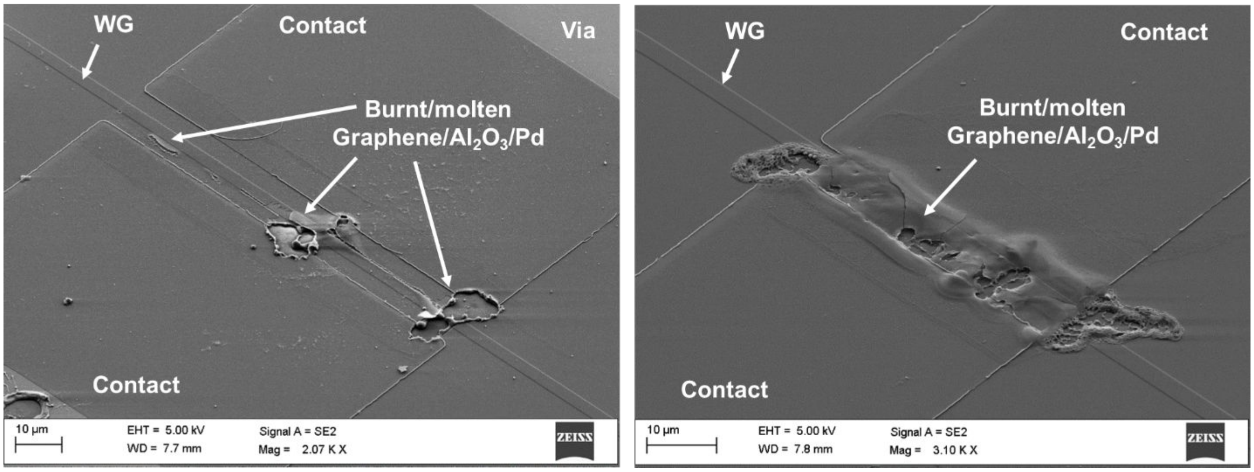

Figure S11. Post-mortem SEM images showing the devices after thermal breakdown.

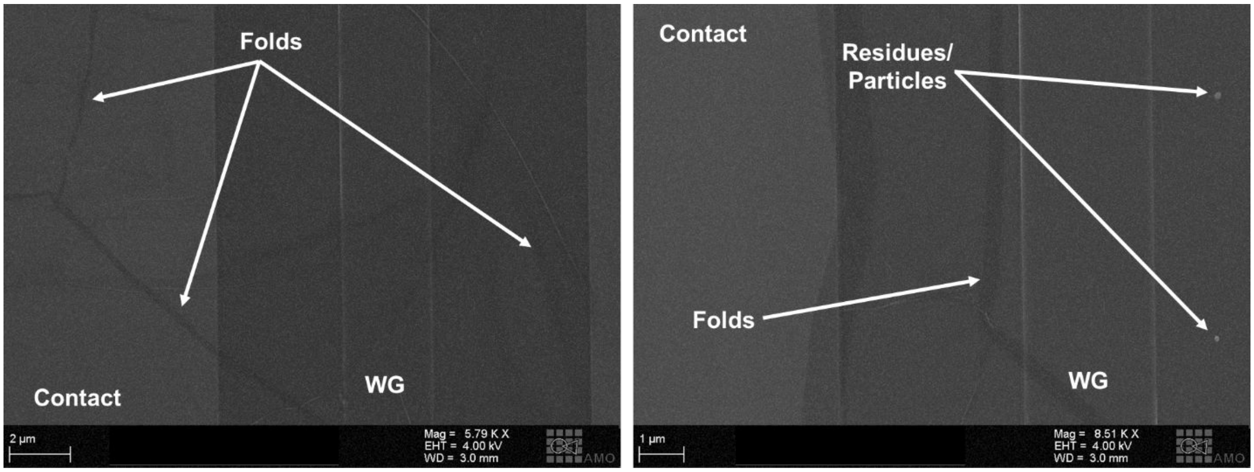

Figure S12. SEM images showing defects in the graphene, such as folds or residues/particles.

ACKNOWLEDGMENTS

This work has received funding from the European Union’s Horizon 2020 research and innovation programme under grant agreement No 825272 (ULISSES) and No 101017186 (AEOLUS).